






RESEARCH ARTICLE | JUNE 20 2023

## Ne, Ar, and Kr oscillators in the molecular cavity of fullerene

C<sub>60</sub>

Tanzeeha Jafari ; Anna Shugai ; Urmas Nagel ; George Razvan Bacanu ; Mohamed Aouane ; Monica Jiménez-Ruiz ; Stéphane Rols ; Sally Bloodworth ; Mark Walkey ; Gabriela Hoffman ; Richard J. Whitby ; Malcolm H. Levitt ; Toomas Rõõm  



*J. Chem. Phys.* 158, 234305 (2023)

<https://doi.org/10.1063/5.0152628>



CrossMark



The Journal of Chemical Physics  
Special Topic: Adhesion and Friction  
Submit Today!



# Ne, Ar, and Kr oscillators in the molecular cavity of fullerene C<sub>60</sub>

Cite as: J. Chem. Phys. 158, 234305 (2023); doi: 10.1063/5.0152628

Submitted: 31 March 2023 • Accepted: 5 June 2023 •

Published Online: 20 June 2023



View Online



Export Citation



CrossMark

Tanzeeha Jafari,<sup>1</sup> Anna Shugai,<sup>1</sup> Urmas Nagel,<sup>1</sup> George Razvan Bacanu,<sup>2</sup> Mohamed Aouane,<sup>3</sup> Monica Jiménez-Ruiz,<sup>3</sup> Stéphane Rols,<sup>3</sup> Sally Bloodworth,<sup>2</sup> Mark Walkey,<sup>2</sup> Gabriela Hoffman,<sup>2</sup> Richard J. Whitby,<sup>2</sup> Malcolm H. Levitt,<sup>2</sup> and Toomas Rõõm<sup>1,a)</sup>

## AFFILIATIONS

<sup>1</sup>National Institute of Chemical Physics and Biophysics, Tallinn 12618, Estonia

<sup>2</sup>School of Chemistry, University of Southampton, Southampton SO17 1BJ, United Kingdom

<sup>3</sup>Institut Laue-Langevin, BP 156, 38042 Grenoble, France

<sup>a)</sup>Author to whom correspondence should be addressed: [toomas.room@kbfi.ee](mailto:toomas.room@kbfi.ee)

## ABSTRACT

We used THz (terahertz) and INS (inelastic neutron scattering) spectroscopies to study the interaction between an endohedral noble gas atom and the C<sub>60</sub> molecular cage. The THz absorption spectra of powdered A@C<sub>60</sub> samples (A = Ar, Ne, Kr) were measured in the energy range from 0.6 to 75 meV for a series of temperatures between 5 and 300 K. The INS measurements were carried out at liquid helium temperature in the energy transfer range from 0.78 to 54.6 meV. The THz spectra are dominated by one line, between 7 and 12 meV, at low temperatures for three noble gas atoms studied. The line shifts to higher energy and broadens as the temperature is increased. Using a spherical oscillator model, with a temperature-independent parameterized potential function and an atom-displacement-induced dipole moment, we show that the change of the THz spectrum shape with temperature is caused by the anharmonicity of the potential function. We find good agreement between experimentally determined potential energy functions and functions calculated with Lennard-Jones additive pair-wise potentials with parameters taken from the work of Pang and Brisse, J. Chem. Phys. 97, 8562 (1993).

© 2023 Author(s). All article content, except where otherwise noted, is licensed under a Creative Commons Attribution (CC BY) license (<http://creativecommons.org/licenses/by/4.0/>). <https://doi.org/10.1063/5.0152628>

## I. INTRODUCTION

Endofullerenes are a class of supramolecular complexes where atoms or molecules, A, are confined inside the C<sub>60</sub> molecular cage, represented as A@C<sub>60</sub>. An effective method to synthesize endofullerenes in milligram quantities was introduced by Komatsu and co-workers in 2005.<sup>1</sup> They successfully enclosed single H<sub>2</sub> molecules in C<sub>60</sub> cages after a series of organic synthesis steps known as “molecular surgery.” Over the years, the list of endofullerenes produced by molecular surgery<sup>2</sup> has been supplemented by H<sub>2</sub>O@C<sub>60</sub>,<sup>3</sup> HF@C<sub>60</sub>,<sup>4</sup> CH<sub>4</sub>@C<sub>60</sub>,<sup>5</sup> and noble gas endofullerenes.<sup>6–8</sup>

Endofullerenes give an opportunity to study non-covalent interactions between the guest and the molecular cage of C<sub>60</sub>. The confining potential quantizes the translational motion of the guest. In the case of confined molecules, there are additional degrees of rotational and vibrational freedom, which complicate the energy spectrum of A@C<sub>60</sub>. The monatomic noble gas endofullerenes, on

the other hand, are relatively simple systems with only translational degrees of freedom.

Since the discovery of noble gas endofullerenes in the early 1990s by mass spectroscopy,<sup>9</sup> they have been studied using a variety of techniques, such as infrared or THz (terahertz) absorption spectroscopy,<sup>10,11</sup> INS (inelastic neutron scattering),<sup>11</sup> NMR (nuclear magnetic resonance),<sup>6,8,12,13</sup> and others.<sup>14,15</sup> In the work of Takeda *et al.*,<sup>12</sup> the influence of the inserted atom on the lattice parameters was revealed for Ar@C<sub>60</sub>. The <sup>13</sup>C chemical shift of the C<sub>60</sub> cage carbon atoms shows downfield shifts of 0.027, 0.17, 0.39, and 0.95 ppm in He@C<sub>60</sub>,<sup>13</sup> Ar@C<sub>60</sub>,<sup>12</sup> Kr@C<sub>60</sub>,<sup>8,16</sup> and Xe@C<sub>60</sub>,<sup>17</sup> respectively. This trend consisted in the greater interaction of the endohedral atom with fullerene electrons as the size of the guest atom increases. Frunzi *et al.*<sup>18</sup> even concluded that the xenon atom pushes the fullerene electrons outward. The first experimental evidence of confinement-induced internuclear J-coupling was reported by Bacanu *et al.*<sup>13</sup> in <sup>3</sup>He@C<sub>60</sub>.

Several theoretical approximations have been made to calculate the potential energy function of a noble gas atom in the fullerene cage.<sup>11,19–24</sup> One approach to model dispersive interactions between atoms is to use a superposition of Lennard-Jones (LJ) 6-12 potentials. The molecular dynamics of Ne inside  $C_{60}$  was reported by Bug *et al.*<sup>25</sup> where the LJ potential was employed to describe the C–Ne interaction within the flexible cage of  $C_{60}$ . The translational frequency of Ne@ $C_{60}$  was predicted at  $90\text{ cm}^{-1}$ . Pang and Brisse<sup>19</sup> calculated endohedral energies of He, Ne, Kr, Ar, and Xe inside  $C_{60}$  and  $C_{70}$  using LJ functions. They concluded that He and Ne form more stable complexes with  $C_{60}$  due to their smaller van der Waals radii as compared to larger Ar, Kr, and Xe. The potential function of He in  $C_{60}$  calculated by Pang and Brisse reproduces the recently spectroscopically determined potential function remarkably well.<sup>11</sup> However, there have been no experimental data for the potential functions of other noble gas atoms in  $C_{60}$ .

This paper is a continuation of our previous work on He@ $C_{60}$ .<sup>11,24</sup> Here, we report a study of Ne, Ar, and Kr endofullerenes by THz spectroscopy and INS. Although the center-of-mass motion of a neutral atom in free space does not interact with electromagnetic radiation, atoms acquire an induced electric dipole moment upon their interaction with  $C_{60}$ , allowing for the oscillatory center-of-mass motion of an endohedral atom to absorb THz radiation. We report both THz and INS data for Ne@ $C_{60}$ . However, in the case of Ar@ $C_{60}$  and Kr@ $C_{60}$ , only the THz data are presented since the difficulties in the synthesis precluded the production of sufficient samples for INS, in these cases.

In the case of an anharmonic potential, the distance between consecutive energy levels changes as the energy increases. This leads to a “comb” of well-resolved THz absorption peaks at temperatures high enough to populate excited transitional states. Such THz “combs” were prominent in the case of He endofullerenes, where the confining potential is highly anharmonic.<sup>10</sup> In contrast, “combs” of THz peaks were not observed for Ar, Ne, and Kr endofullerenes. As discussed below, this is because the confining potential is much more harmonic than for He.

To study the anharmonicity of the interaction potential, THz absorption spectra were measured over a wide temperature range from 5 to 300 K. The INS spectra were acquired for Ne@ $C_{60}$  at low temperature. The interaction potential parameters were determined by fitting the experimental spectra to a spherical anharmonic oscillator model. Finally, the experimentally derived potential functions were compared with predictions using the LJ two-body potential parameters of Pang and Brisse.<sup>19</sup>

## II. MATERIALS AND METHODS

### A. Sample preparation

Endofullerenes containing Ne, Ar, and Kr atoms were synthesized by multi-step “molecular surgery.” The shell of  $C_{60}$  is chemically opened to create an orifice. The orifice should be of proper size to allow for the entering of a guest atom and at the same time to prevent its quick loss. An open-cage intermediate fullerene incorporating atom is closed with a sequence of chemical reactions. Ar@ $C_{60}$  and Kr@ $C_{60}$ <sup>6,8</sup> were made using a similar sequence of chemical reactions for the contraction and the closure of the open-cage endofullerene orifice. For Ne@ $C_{60}$ , the open-cage fullerene was filled by Ne gas in the solid state and the Ne atom was trapped through the solid-state

Wittig reaction induced by raising the temperature.<sup>7</sup> It was found that traces of a  $H_2O@C_{60}$  impurity interfered with INS measurements due to the strong incoherent scattering of water protons. This impurity was removed from the Ne@ $C_{60}$  sample by extensive HPLC (high-performance liquid chromatography). To improve the signal-to-noise ratio of THz spectroscopy, the filling factor of the samples was further increased by extensive recirculating HPLC. The achieved filling factors  $f$  (defined as the fraction of  $C_{60}$  cages containing an endohedral guest) are given below. All samples were sublimed under vacuum before spectroscopic measurements.

### B. Terahertz spectroscopy

The powdered samples of  $A@C_{60}$  were pressed under vacuum into 3 mm diameter pellets to perform THz measurements. The pellet thicknesses of Ne@ $C_{60}$ , Ar@ $C_{60}$ , and Kr@ $C_{60}$  were 1.61, 1.06, and 0.95 mm, and the filling factors were 0.99, 1.0, and 1.0. The sample masses were estimated to be 21.5, 13.2, and 12.3 mg for Ne@ $C_{60}$ , Ar@ $C_{60}$ , and Kr@ $C_{60}$ , respectively.

The transmission spectra of Ar@ $C_{60}$  and Kr@ $C_{60}$  were recorded using a vacuum FTIR Bruker spectrometer (Vertex 80v). A standard far-infrared setup covering the range from 10 to  $600\text{ cm}^{-1}$  was used for the measurements: an electrically heated SiC (Glo-bar) radiation source, a  $6\text{ }\mu\text{m}$  thick Mylar beam splitter, and a 4 K bolometer for detection. In order to reach low temperatures, a compact cold-finger continuous flow cryostat was used. The required temperature within the cryostat was maintained by controlling the flow of helium and by using the heater. To register the transmission spectra, the cryostat insert with the cold finger moves up and down, allowing the signal to pass through the sample or through a 3 mm diameter hole as a reference channel. The sample channel was equipped with a sample cell with two polypropylene windows that kept the sample in an atmosphere of helium exchange gas. This technique allowed for good thermal contact between the cold-finger and the pellet.

The Ne@ $C_{60}$  spectra were measured from 5 up to  $100\text{ cm}^{-1}$  using a Martin–Puplett interferometer equipped with a high-pressure Hg lamp as a radiation source. The chamber of the  $^3\text{He}$  cooled bolometer (working temperature  $T = 0.3\text{ K}$ ) and the sample chamber were immersed in a liquid helium bath. The sample and reference hole shared the same He heat exchange gas environment. The sample temperature  $T$  was controlled by the heater and the exchange gas pressure. The resolution used on both instruments was  $0.3\text{ cm}^{-1}$ , which is less than the linewidth of the measured absorption lines for the studied samples. The calculations of the THz absorption spectra of  $A@C_{60}$  and the baseline corrections are described in the supplementary material.

### C. Inelastic neutron scattering

INS experiments were conducted using the IN1-Lagrange spectrometer at the Institut Laue–Langevin (ILL) in Grenoble. Incident neutrons are provided by the “hot source” moderator of the reactor, resulting in a high flux neutron beam. Selection of three different single crystal monochromators, namely, Si(111), Si(311), and Cu(220), enables selection of the incident energy of the monochromatic neutron beam arriving at the sample by using Bragg reflection. The neutrons scattered by the sample enter a secondary spectrometer comprising a large area array of pyrolytic graphite analyzer

crystals. The focusing geometry of the secondary spectrometer ensures that only neutrons with a fixed kinetic energy of 4.5 meV are detected by using the  $^3\text{He}$  detector. INS spectra were recorded in the energy transfer range from 0.78 to 54.6 meV. The 170 mg  $\text{Ne}@C_{60}$  powder,  $f = 0.7$ , was wrapped in a thin aluminum pocket and attached to the tip of the cryostat. The  $\text{Ne}@C_{60}$  spectra were corrected for the scattering from the aluminum foil and from  $C_{60}$  (supplementary material).

#### D. Model and parameter fitting

The details of the spherical oscillator model of an atom encapsulated by  $C_{60}$  can be found in Refs. 11 and 24. Here, we highlight the key aspects.  $C_{60}$  is treated as a rigid body with a fixed center of mass. This excludes temperature effects on the confining potential caused by  $C_{60}$  molecular vibrations, crystal lattice modes, and crystal lattice thermal expansion. In principle, the confining potential inherits icosahedral symmetry from the symmetry of the fullerene cage. For simplicity, we neglect the deviations from spherical symmetry and expand the spherically symmetrical potential in even powers of  $r$ , defined as the displacement of the endohedral atom from the cage center,

$$\hat{V}(r) = \sum_{k=2}^{\infty} V_k r^k. \quad (1)$$

The harmonic spherical oscillator Hamiltonian,

$$\hat{H} = -\frac{\hat{p}^2}{2m} + V_2 r^2, \quad (2)$$

has been solved analytically;<sup>26</sup>  $p$  and  $m$  are the momentum and mass of the atom. The radial quantum number  $n$  and the orbital quantum number  $\ell$  characterize the eigenstates and eigenvalues (energy levels) of the Hamiltonian (2), where  $\ell$  takes even values from 0 to  $n$  for even  $n$  and odd values from 1 to  $n$  for odd  $n$ . The energies of a harmonic spherical oscillator are given by  $E_{n\ell} = \hbar\omega_0(n + 3/2)$  and  $\omega_0 = \sqrt{2V_2/m}$ . The Hamiltonian including anharmonic terms  $V_k$ ,  $k > 2$ , is diagonalized numerically using a finite-size basis of the harmonic Hamiltonian eigenstates. Here, we used eigenstates up to the quantum number  $n_{\text{max}} = 18$ . Because the potential is approximated as being spherical, there is no mixing of states with different  $\ell$  values and the energy levels remain  $(2\ell + 1)$ -fold degenerate.

To fit the THz absorption line intensities of translational transitions, we assume that the dipole moment is induced by the displacement of an atom from the  $C_{60}$  cage center,  $\mathbf{r} = (r, \phi, \theta)$ , as expressed in spherical coordinates. As discussed in Ref. 24, the displacement-induced electric dipole moment may be expressed in terms of rank-1 spherical harmonics as follows:

$$d_{1q} = \sqrt{\frac{4\pi}{3}} \sum_{p=1}^{\infty} A_{pq} r^p Y_{1q}(\theta, \phi), \quad (3)$$

where  $A_{pq}$  is the dipole amplitude coefficient and  $q \in \{-1, 0, +1\}$ . Within the approximation of spherical symmetry,  $A_{pq}$  is independent of  $q$ ,  $A_{pq} = A_p$ . Furthermore, since the dipole moment is a polar vector, only odd powers of  $r$  are involved, i.e.,  $p \in \{1, 3, \dots\}$ . For the atoms studied here, it was found that the terms linear in  $r$  (i.e.,  $p = 1$ ) are sufficient. Cubic and higher-order terms were ignored

in the fit. The selection rule for transitions between the spherical oscillator levels induced by the electric field coupled to the dipole moment, Eq. (3), linear in  $r$  is  $\Delta\ell = \pm 1$  and  $\Delta n = \pm 1$ .<sup>24</sup> The relationship between the THz absorption coefficients and the matrix elements of the induced dipole moment, including the thermal populations of the oscillator levels, is given in Ref. 24.

The fitted parameters,  $\{V_2, V_4, A_1\}$ , are found by minimizing the difference-squared of the calculated spectrum and the baseline-corrected experimental spectrum. In the cases where there is more than one isotope, the diagonalization and the dipole matrix calculation are carried out separately for each mass. The spectra of isotopes are added using the natural abundances as weighting factors. The minimization is done simultaneously over several temperatures assuming temperature-independent linewidths of the calculated peaks. Parameter confidence limits are calculated using the method described in Ref. 27.

#### E. Potential energy functions from the Lennard-Jones model

The Lennard-Jones (LJ) 6-12 potential describes the interaction energy between two atoms as a function of their distance of separation with two empirical parameters; see, e.g., Ref. 21. In the case of  $A@C_{60}$ , the potential energy function for the  $A$  atom is calculated by displacing atom  $A$  from the center of the fullerene cage by  $r$  and summing over sixty A-C two-body interactions for each position  $r$ . LJ confining potentials given in this article are obtained by moving the noble gas atom toward the center of a HH bond (the bond in between two hexagons). As shown in the supplementary material, the direction of the displacement of the atom from the center of the cage has very little effect on the potential. As reported in Ref. 11, the positions of the  $C_{60}$  atoms were fixed to the best known values as calculated from the neutron scattering data.<sup>28</sup> The given structural parameters are  $r_0 = 354.7 \pm 0.5$  pm, the distance of all carbon nuclei from the center of the cage;  $h = 138 \pm 0.27$  pm, the bond length that joins hexagonal  $C_6$  rings; and  $p = 145.97 \pm 0.18$  pm, the bond length that joins  $C_6$  and pentagonal  $C_5$  rings. The parameters of Pang and Brisse,<sup>19</sup> corrected by Jiménez-Vázquez and Cross,<sup>21</sup> were used for all LJ potentials.

### III. RESULTS

#### A. $\text{Ne}@C_{60}$

$\text{Ne}@C_{60}$  absorption spectra are shown as a function of temperature in Fig. 1. At 3 K, we see a strong peak at  $56.6 \text{ cm}^{-1}$ , which according to our model calculation is the transition from the ground state  $n = 0$  to the first excited translational state  $n = 1$ ; see Table II. The shape of this main line at 3 K is described by a Lorentzian function, with  $0.5 \text{ cm}^{-1}$  full width at half maximum (FWHM).

The position of the main peak changes when  $T$  increases from 3 to 40 K (see the inset of Fig. 1) and also the line broadens. The absorption spectrum continues to shift and broaden at higher temperatures, as shown in Fig. 1. This effect is attributed to the increasing population of higher translational states at higher temperatures, combined with the significant anharmonicity of the potential. Because our model does not explain the temperature dependence observed below 30 K, the spectra measured at following  $T$  were used to fit the potential and dipole moment parameters: 30, 40, 50, 60, 70,

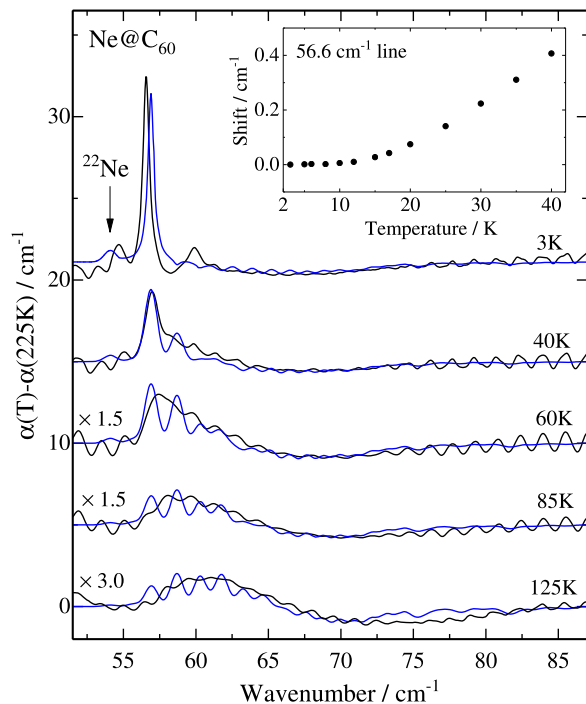


**FIG. 1.** THz differential absorption spectra of Ne@C<sub>60</sub> at different temperatures (black) and the differential spectra calculated with the best fit parameters from Table I (blue). The line shape is assumed to be Lorentzian at 3 K (FWHM = 0.5 cm<sup>-1</sup>) and Gaussian (FWHM = 1.0 cm<sup>-1</sup>) for temperatures of 40 K and higher. The intensities of the 60, 85, and 125 K differential spectra have been multiplied by factors of 1.5 and 3. The inset shows the temperature dependence of the main peak frequency shift,  $\omega_{01}(T) - \omega_{01}(3\text{ K})$ , between 3 and 40 K.

85, 100, 125, 150, and 175 K. For the model fitting, these spectra were referenced to the 225 K spectrum. Similarly, the spectra calculated with the model parameters were referenced to the model spectrum at 225 K. The difference spectra,  $\alpha(T) - \alpha(225\text{ K})$ , calculated with the best fit model parameters, given in Table I, are plotted in Fig. 1. The oscillations seen in the calculated spectra are individual lines

resolved by FWHM = 1.0 cm<sup>-1</sup> used for plotting. The <sup>22</sup>Ne peak, natural abundance 9.3%,<sup>29</sup> is clearly seen on the lower frequency side of the main <sup>20</sup>Ne peak in the calculated spectra. The <sup>22</sup>Ne peak is obscured in the experimental spectra by baseline artifacts associated with the subtraction of spectra taken at widely different temperatures, Fig. 1. This peak is more visible in the  $\alpha(T) - \alpha(100\text{ K})$  difference spectra; see Fig. S5 of the supplementary material. However, its frequency differs slightly from the anticipated isotope shift; see Sec. IV.

The low *T* INS spectrum of Ne@C<sub>60</sub> is plotted in Fig. 2. The peak at 7 meV and the THz peak at 56.6 cm<sup>-1</sup> coincide well within the width of the INS peak. Although there is a peak in the INS spectrum at 13 meV, its energy is too low to be assigned to the  $n = 0 \rightarrow n = 2$  transition. Other two peaks above 13 meV, coinciding with  $n = 0 \rightarrow n = 2$  transitions, are too weak compared to the noise to be assigned to Ne@C<sub>60</sub> transitions (supplementary material).

### B. Ar@C<sub>60</sub>

The temperature-dependence of the THz absorption spectra of Ar@C<sub>60</sub> is shown in Fig. 3. The 5 K spectrum displays one sharp peak at 91.9 cm<sup>-1</sup>. The shape of the peak up to 50 K is best described by a Lorentzian line shape with FWHM = 0.5 cm<sup>-1</sup>. As the temperature increases, the absorption peak broadens and its maximum shifts to higher frequency. This is due to the increasing population of higher translational states at higher temperatures, combined with the significant anharmonicity of the potential. The experimental spectra were fitted at 5, 10, 20, 30, 40, 50, 60, 80, 100, 140, 180, 220, 250, 270, and 300 K using the Lorentzian shape with FWHM = 0.5 cm<sup>-1</sup>. The spectra calculated with the best fit parameters from Table I and plotted in Fig. 3 show that the experimentally observed *T* dependence of the spectrum is well described by an anharmonic potential.

### C. Kr@C<sub>60</sub>

Unlike Ne@C<sub>60</sub> and Ar@C<sub>60</sub>, the Kr@C<sub>60</sub> spectrum shows a broad asymmetrical absorption line even at 5 K, Fig. 4. At higher temperatures, the Kr@C<sub>60</sub> spectrum broadens further and its maximum shifts to higher frequency, similar to the behavior of Ne and Ar. The fit of the experimental absorption spectra of Kr@C<sub>60</sub> was done at temperatures of 5, 40, 80, 120, 160, 200, 240, 280, and 310 K

**TABLE I.** Best fit polynomial coefficients and confidence limits for the radial potential function  $V(r) = V_2r^2 + V_4r^4 + V_6r^6$  and induced dipole function  $d_{1q} = (4\pi/3)^{1/2}(A_1r + A_3r^3)Y_{1q}(\theta, \phi)$  of the confined atoms.  $\omega_{01}$  is the peak frequency of the absorption line at 5 K in the measured THz spectrum corresponding to the  $n = 0 \rightarrow n = 1$  transition.  $v_{\text{anh}} = (\omega_{01} - \omega_0)/\omega_{01}$  is the fractional contribution of the anharmonic potential to  $\omega_{01}$ , where  $\omega_0 = \sqrt{2V_2/m}$  is the frequency of the harmonic oscillator, *m* is the mass of the endohedral atom, and *c* is the speed of light in vacuum. The <sup>4</sup>He@C<sub>60</sub> data are from Ref. 24.

Parameter	<sup>4</sup> He	<sup>20</sup> Ne	<sup>40</sup> Ar	<sup>84</sup> Kr
$V_2$ (J m <sup>-2</sup> )	0.39 ± 0.006	1.58 ± 0.04	9.56 ± 0.03	17.81 ± 0.12
$V_4$ (J m <sup>-4</sup> )	(0.60 ± 0.01) × 10 <sup>20</sup>	(2.28 ± 0.22) × 10 <sup>20</sup>	(8.19 ± 0.16) × 10 <sup>20</sup>	(13.2 ± 1.60) × 10 <sup>20</sup>
$V_6$ (J m <sup>-6</sup> )	(3.94 ± 0.09) × 10 <sup>39</sup>	0	0	0
$A_1$ (C)	(0.68 ± 0.04) × 10 <sup>-21</sup>	(1.84 ± 0.13) × 10 <sup>-21</sup>	(3.31 ± 0.01) × 10 <sup>-21</sup>	(3.30 ± 0.21) × 10 <sup>-21</sup>
$A_3$ (Cm <sup>-2</sup> )	0.04 ± 0.01	0	0	0
$(2\pi c)^{-1}\omega_{01}$ (cm <sup>-1</sup> )	81.4	56.6	91.8	85.4
$v_{\text{anh}}$	0.29	0.085	0.018	0.007

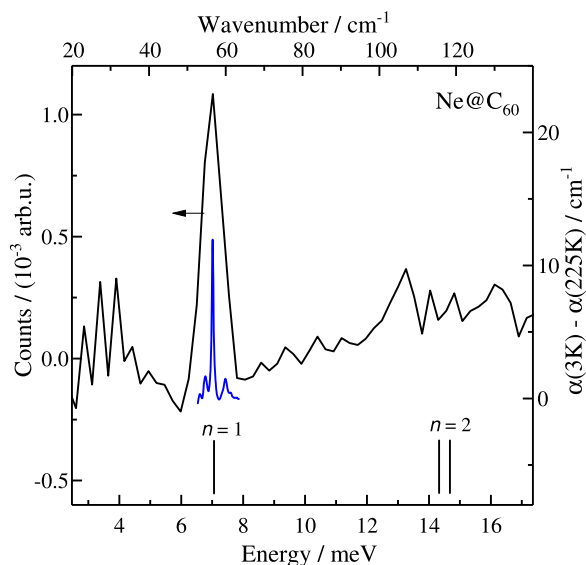


**FIG. 2.** INS spectrum of Ne@C<sub>60</sub> at 2.7 K (black). The INS signal of empty C<sub>60</sub> is subtracted. Sticks denote the predicted energies of the transitions from the ground state  $n = 0$  to the first ( $n = 1, \ell = 1$ ) and to the second translational level ( $n = 2, \ell = 2$ , and  $\ell = 0$ ), Table II, calculated from the anharmonic oscillator model using the best fit parameters of the THz absorption spectra, Table I. The THz spectrum at 3 K is plotted for comparison, blue line.

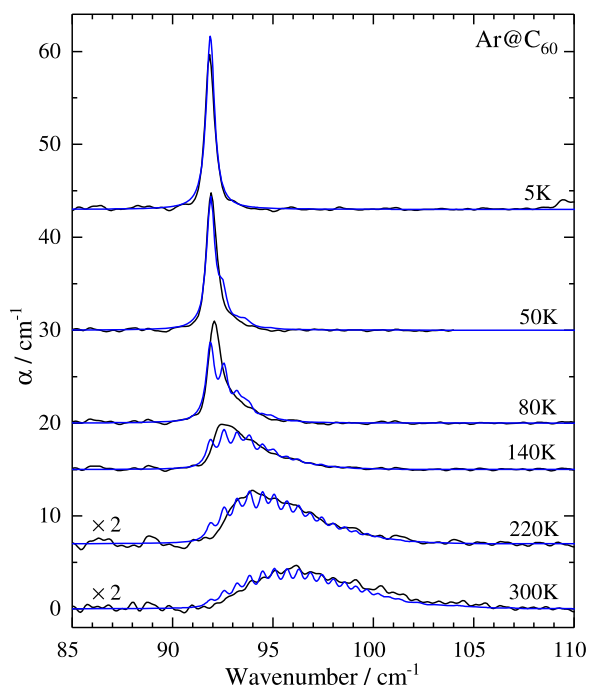


**FIG. 3.** THz absorption spectra of Ar@C<sub>60</sub> at different temperatures (black) and the spectra calculated with the best fit parameters from Table I and plotted with a Lorentzian line shape, FWHM = 0.5 cm<sup>-1</sup> (blue). The 220 and 300 K spectra are multiplied by a factor of 2.

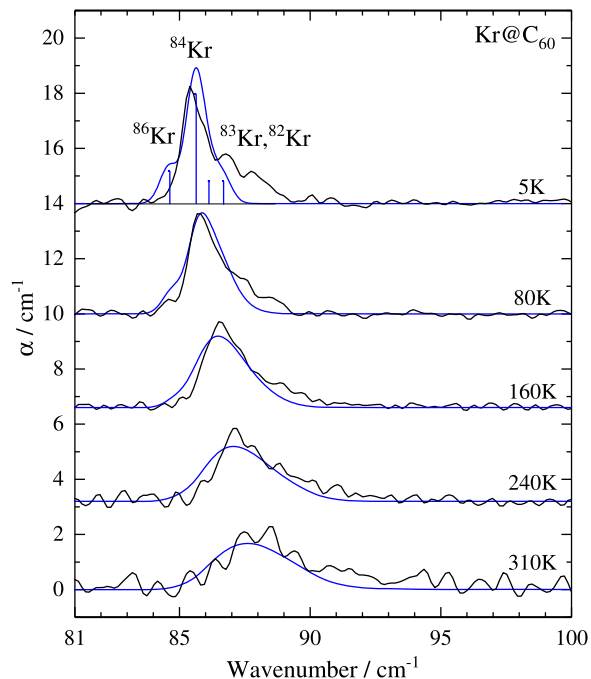


**FIG. 4.** THz absorption spectra of Kr@C<sub>60</sub> at different temperatures (black) and the spectra calculated with the best fit parameters from Table I and plotted using a Gaussian line shape with FWHM = 0.8 cm<sup>-1</sup> (blue). The simulated spectra for the four most abundant isotopes are included, weighted by their natural abundances. The sticks indicate the isotopic composition of the 5 K spectrum.

with FWHM = 0.8 cm<sup>-1</sup> for all isotopes. The spectra calculated with the best fit parameters from Table I are plotted in Fig. 4. Compared to Ne and Ar, the calculated spectra of Kr do not show oscillations because first the spread of line frequencies in the high temperature spectra is less for Kr@C<sub>60</sub> due to a smaller anharmonicity and second the FWHM of individual lines is larger in the calculated spectra of Kr@C<sub>60</sub>. The asymmetric line shape at 5 K is partially caused by the isotope distribution of Kr: <sup>82</sup>Kr – 11.6%, <sup>83</sup>Kr – 11.5%, <sup>84</sup>Kr – 57%, and <sup>86</sup>Kr – 17.3%, counting the four most abundant isotopes.<sup>29</sup> The model predicts extra absorption on both sides of the most abundant isotope peak at 5 K but does not account for all absorption on the higher frequency side of that peak, as discussed in Sec. IV.

#### IV. DISCUSSION

The spherical oscillator parameters that provide the best match to the experimental THz spectra, and their confidence limits, are summarized in Table I. In all cases, the anharmonic terms  $V_4$  are positive, which means that the separation between the energy levels increases with the increasing energy. Unlike the highly anharmonic case of He@C<sub>60</sub> (see the fractional anharmonicity  $\nu_{\text{anh}}$  in Table I), for which the transitions from different starting levels are resolved in the THz spectrum at high temperature, the transitions for Ne, Ar, and Kr merge into one broad line. Since the separation between the energy levels increases with the increasing energy, this broad spectral line shifts to higher energy with the increasing temperature as

**TABLE II.** Translational energy levels of  $^{20}\text{Ne}@C_{60}$ ,  $^{40}\text{Ar}@C_{60}$ , and  $^{84}\text{Kr}@C_{60}$  calculated with the parameters given in Table I, which provide the best correspondence between the THz absorption spectra and the anharmonic spherical oscillator model. The columns give the translational energy  $E$ , the angular momentum quantum number  $\ell$  (single-valued for each energy level), and the amplitude-squared  $|\xi_n|^2$  of the main component of the eigenstate with the principal quantum number  $n$ . The tabulated energies are relative to the zero-point energies, which are as follows:  $81.75\text{ cm}^{-1}$  for  $^{20}\text{Ne}@C_{60}$ ,  $136.52\text{ cm}^{-1}$  for  $^{40}\text{Ar}@C_{60}$ , and  $127.86\text{ cm}^{-1}$  for  $^{84}\text{Kr}@C_{60}$ .

$^{20}\text{Ne}@C_{60}$				$^{40}\text{Ar}@C_{60}$				$^{84}\text{Kr}@C_{60}$			
$E\text{ (cm}^{-1}\text{)}$	$n$	$\ell$	$ \xi_n ^2$	$E\text{ (cm}^{-1}\text{)}$	$n$	$\ell$	$ \xi_n ^2$	$E\text{ (cm}^{-1}\text{)}$	$n$	$\ell$	$ \xi_n ^2$
0	0	0	1.0	0	0	0	1.0	0	0	0	1.0
56.9	1	1	0.99	91.9	1	1	1.0	85.6	1	1	1.0
115.6	2	2	0.98	184.4	2	2	1.0	171.5	2	2	1.0
118.4	2	0	0.97	185.4	2	0	1.0	171.9	2	0	1.0
175.9	3	3	0.96	277.6	3	3	1.0	257.7	3	3	1.0
180.3	3	1	0.93	279.3	3	1	1.0	258.4	3	1	1.0
237.7	4	4	0.94	371.5	4	4	1.0	344.1	4	4	1.0
243.5	4	2	0.89	373.8	4	2	0.99	345.1	4	2	1.0
246.0	4	0	0.87	374.8	4	0	0.99	345.6	4	0	1.0
301.0	5	5	0.92	466.0	5	5	1.0	430.9	5	5	1.0
308.1	5	3	0.89	468.9	5	3	0.99	432.2	5	3	1.0
312.0	5	1	0.79	470.5	5	1	0.99	432.9	5	1	1.0
365.6	6	6	0.89	561.1	6	6	0.99	517.9	6	6	1.0
373.9	6	4	0.77	564.6	6	4	0.98	519.5	6	4	1.0
379.2	6	2	0.70	566.8	6	2	0.98	520.5	6	2	1.0
381.4	6	0	0.67	567.8	6	0	0.98	520.9	6	0	1.0
431.5	7	7	0.86	656.8	7	7	0.99	605.2	7	7	1.0
440.8	7	5	0.70	660.9	7	5	0.98	607.0	7	5	1.0
447.4	7	3	0.60	663.7	7	3	0.97	608.3	7	3	0.99
451.0	7	1	0.56	665.3	7	1	0.97	609.0	7	1	0.99
498.6	8	8	0.82	753.1	8	8	0.99	692.8	8	8	1.0
509.0	8	6	0.62	757.8	8	6	0.97	694.9	8	6	0.99
516.7	8	4	0.50	761.2	8	4	0.96	696.4	8	4	0.99
521.6	8	2	0.43	763.4	8	2	0.95	697.4	8	2	0.99
523.7	8	0	0.41	764.3	8	0	0.95	697.8	8	0	0.99
566.9	9	9	0.79	850.0	9	9	0.98	780.6	9	9	1.0
578.2	9	7	0.40	855.2	9	7	0.96	783.0	9	7	0.99
587.0	9	5	0.40	859.2	9	5	0.94	784.8	9	5	0.99
593.1	11	3	0.39	862.0	9	3	0.93	786.0	9	3	0.98
596.5	11	1	0.4	863.6	9	1	0.93	786.7	9	1	0.98

observed for Ne, Ar, and Kr. The anharmonic term of the potential,  $V_4$ , mixes states with different  $n$  but the same  $\ell$  in the approximation of spherical symmetry. The amplitude squared,  $|\xi_n|^2$ , of the dominant harmonic oscillator state with the principal quantum number  $n$  is given in Table II. In the case of Ne, the  $|\xi_n|^2$  factor decreases as  $n$  increases, reflecting the significant anharmonicity of the potential, which mixes states with different  $n$  quantum numbers. For Kr, on the other hand, there is little mixing, which corresponds to a low level of anharmonicity. The behavior of Ar is intermediate.

In Fig. 5, we compare the best-fit anharmonic interaction potentials  $V(r)$  with the potentials derived by a summation of LJ two-body terms using the parameters of Pang and Brisse.<sup>19</sup> The best-fit anharmonic oscillator potential and the LJ potential agree best for the case of Ne@C<sub>60</sub>. Other atoms show minor discrepancies between the best-fit anharmonic oscillator potential and the LJ potential curves. In general, the LJ potentials with parameters from Pang and Brisse<sup>19</sup> agree surprisingly well with the experimental data,

especially considering the delocalized electronic structure of C<sub>60</sub>. As can be seen in Fig. 5, the potential curves become increasingly steep when going from He to Kr, which is consistent with the larger size of the atoms.

Despite the overall good agreement between the theoretical model and the experimental data, some discrepancies remain. These include the following: (1) An anomalous temperature-dependent shift of the main THz absorption peak of Ne@C<sub>60</sub> at temperatures below 30 K is seen, Fig. 1 (inset). This low-temperature frequency shift is not predicted by the theoretical model, in contrast to the behavior at higher temperatures, which does appear to be well-predicted. (2) In some cases, the difference in translational frequency for isotopes of different masses is not in full agreement with theoretical expectations. This is the case for the  $^{22}\text{Ne}$  and  $^{20}\text{Ne}$  peaks, Fig. 1. (3) In some cases, an additional structure is observed above the main THz absorption peak frequency, e.g., a peak at  $60\text{ cm}^{-1}$  in the Ne@C<sub>60</sub> spectrum, Fig. 1. Although we do not have a full explanation

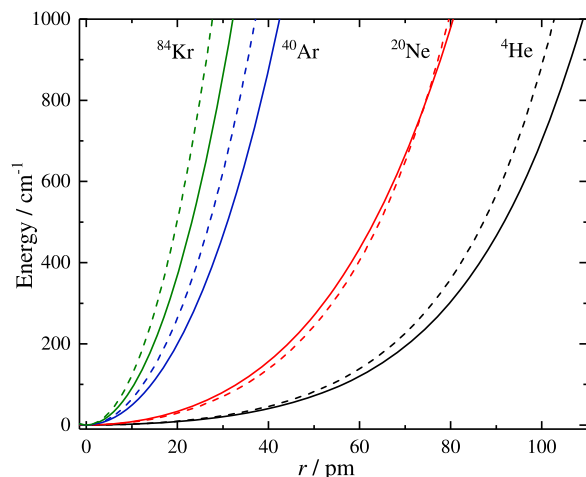


**FIG. 5.** Comparison of the experimentally determined potential functions  $V(r)$  and the LJ potential functions of  ${}^4\text{He}@C_{60}$ ,  ${}^{20}\text{Ne}@C_{60}$ ,  ${}^{40}\text{Ar}@C_{60}$ , and  ${}^{84}\text{Kr}@C_{60}$ . Solid lines: Potential energy curves for the anharmonic spherical oscillator model, with parameters given in Table I, which provide the best fit to the experimental data. Dashed lines: Potential energy curves obtained by summing Lennard-Jones two-body potentials, with parameters given in Ref. 19.

of all of these features, the following factors may be considered: (1) Temperature-dependent phase transitions and lattice parameters for crystalline  $C_{60}$ . (2) Merohedral disorder. (3) Interference between the translational modes of the endohedral atom and inter-molecular lattice modes.

Crystalline  $C_{60}$  has a first-order phase transition from the face-centered cubic phase above 260 K to a simple cubic structure below 260 K.<sup>30</sup> The lattice constant decreases gradually with temperature with a jump at 260 K and a small kink at about 90 K. Below 90 K, there is a frozen-in merohedral disorder. The two orientations, named hexagonal and pentagonal, are distinguished by the relative orientation of the central cage and its 12 nearest-neighbor  $C_{60}$  molecules. About 85% of  $C_{60}$  molecules have their electron-rich double bond facing the pentagonal face and 15% have the same bond facing the hexagonal face of a neighboring molecule.<sup>30,31</sup>

The phonon density of states has a gap between  $\sim 70$  and  $240\text{ cm}^{-1}$ .<sup>32</sup> The phonons below  $70\text{ cm}^{-1}$  have mainly inter-molecular character, and those above  $240\text{ cm}^{-1}$  have mainly intra-molecular character.

The anomalous temperature-dependent shift of the main THz absorption peak of  $\text{Ne}@C_{60}$  at temperatures below 30 K might be associated with the interference between the translational modes of the endohedral atom and inter-molecular lattice modes. The low-temperature shift is not observed for helium<sup>24</sup> nor for argon, Fig. 3, which is consistent with the observation that the translational frequencies of these two atoms are above the density of states of inter-molecular phonons of crystalline  $C_{60}$ . For Ne, on the other hand, there is a clear overlap of the translational peak with the region of high phonon density, as can be seen in the INS spectrum (supplementary material). The interaction with inter-molecular lattice modes may also explain why the frequencies of the  ${}^{20}\text{Ne}$  and  ${}^{22}\text{Ne}$  translational peaks do not agree with the theoretical prediction.

The additional structure above the main absorption peak at low temperature could be explained by merohedral disorder. It was shown theoretically that the two lattice orientations of  $C_{60}$  molecules produce different electric field gradients at the  $C_{60}$  cage centers. The interaction of these electric field gradients with the molecular quadrupole moments splits the rotational levels of endohedral molecules.<sup>33</sup> Although the noble gas atoms lack a quadrupole moment, it is possible that the atom has a different potential function, Eq. (1) in the hexagonal and pentagonal sites. There are two experimental observations that support this idea in the case of  $\text{Ne}@C_{60}$ . First, the behavior of the  $\text{Ne}@C_{60}$   $60\text{ cm}^{-1}$  line is consistent with transitions starting from the ground state (supplementary material). Second, the ratio of the areas of  $56.6$  and  $60\text{ cm}^{-1}$  peaks for  $\text{Ne}@C_{60}$  is 8:2 (supplementary material), which is consistent with the relative population of pentagonal and hexagonal sites in  $C_{60}$  at low temperature.<sup>30</sup> The temperature dependence and the spectral weight of the  $87\text{ cm}^{-1}$  line of  $\text{Kr}@C_{60}$  are not possible to evaluate reliably because it overlaps with the spectral lines of the main site. We have no experimental evidence that  $\text{Ar}@C_{60}$  has any side peaks that can be related to the minority site, Fig. 3. However, a clear minority side-peak was observed for  $\text{He}@C_{60}$ .<sup>24</sup>

To summarize, we have observed THz peaks from the translation of Ne, Ar, and Kr atoms inside fullerene cages. The THz spectra, and their temperature-dependence, are mainly consistent with confinement of the atoms by an anharmonic spherical potential. The translational frequency of He, Ar, and Kr is close to  $90\text{ cm}^{-1}$  (2.7 THz) although the mass changes by a factor of 20 from He to Kr. This is because the increase in mass of the endohedral atom and its accompanying increase in size lead to opposite influences on the translational frequency. The increase in mass decreases the translational frequency, while the increases in size leads to a steeper confining potential, which increases the translational frequency. The combination of mass and atom size sets  $\text{Ne}@C_{60}$  to the lower frequency side from other atoms to  $57\text{ cm}^{-1}$ . The anharmonic part of the potential is positive,  $V_4 > 0$ , and the anharmonicity weakens with the increase of the atom size. Since the anharmonicity of the heavier atoms is not as large as for the lighter helium, the peaks are not resolved in the spectrum, and instead, the anharmonicity leads to a broadening and shift of the peak to higher frequency with an increase in temperature.

## SUPPLEMENTARY MATERIAL

The supplementary material includes technical details of the inelastic neutron scattering measurements and the subtraction of the empty  $C_{60}$  spectrum from the  $\text{Ne}@C_{60}$  spectrum; the details of how the THz absorption spectra were calculated and the baseline subtracted and additional data about  $\text{Ne}@C_{60}$  spectra are included; and the induced dipole moments of atoms that are compared and the dependence of LJ potential curves on the direction of atom displacement that is plotted.

## ACKNOWLEDGMENTS

This research was supported by the Estonian Ministry of Education, personal research funding PRG736; the European Regional Development Fund, Project No. TK134; and EPSRC under Grant Nos. EP/P009980/1 and EP/T004320/1 of UK. Use of the INS



spectroscopy setup was granted by the ILL through Proposal No. 7-04-176 (doi:10.5291/ILL-DATA.7-04-176). M.A. acknowledges the ILL for a financial support.

## AUTHOR DECLARATIONS

### Conflict of Interest

The authors have no conflicts to disclose.

### Author Contributions

M.W., G.H., S.B., and R.J.W. carried out synthesis and purification of endofullerenes. G.R.B., M.J.-R., M.A., and S.R. performed the INS experiments and processed the INS data. T.J., A.S., U.N., and T.R. performed the THz experiments and processed the THz data. T.J., A.S., and T.R. derived the potential parameters by fitting the THz spectra. G.R.B. calculated the LJ potential functions. T.J. and A.S. wrote an initial draft of the paper. T.R. and M.H.L. developed the concept of the paper. All authors reviewed the manuscript.

**Tanzeeha Jafari:** Data curation (equal); Formal analysis (equal); Visualization (equal); Writing – original draft (equal); Writing – review & editing (equal). **Anna Shugai:** Data curation (equal); Formal analysis (equal); Visualization (equal); Writing – original draft (equal); Writing – review & editing (equal). **Urmaz Nagel:** Funding acquisition (equal); Resources (equal); Software (lead); Writing – review & editing (equal). **George Razvan Bacanu:** Data curation (equal); Formal analysis (equal); Methodology (equal); Visualization (equal); Writing – review & editing (equal). **Mohamed Aouane:** Data curation (equal); Formal analysis (equal); Writing – review & editing (supporting). **Monica Jiménez-Ruiz:** Data curation (equal); Formal analysis (equal); Writing – review & editing (supporting). **Stéphane Rols:** Data curation (equal); Formal analysis (equal); Funding acquisition (equal); Resources (equal); Supervision (equal); Writing – review & editing (equal). **Sally Bloodworth:** Resources (equal); Writing – review & editing (equal). **Mark Walkey:** Resources (equal); Writing – review & editing (supporting). **Gabriela Hoffman:** Resources (equal); Writing – review & editing (supporting). **Richard J. Whitby:** Funding acquisition (equal); Resources (equal); Supervision (equal); Writing – review & editing (equal). **Malcolm H. Levitt:** Conceptualization (equal); Funding acquisition (equal); Project administration (equal); Supervision (equal); Validation (equal); Writing – original draft (equal); Writing – review & editing (equal). **Toomas Rõõm:** Conceptualization (equal); Funding acquisition (equal); Methodology (equal); Project administration (equal); Resources (equal); Supervision (equal); Validation (equal); Writing – original draft (equal); Writing – review & editing (equal).

## DATA AVAILABILITY

The data that support the findings of this study are available from the corresponding author upon reasonable request.

## REFERENCES

- 1 K. Komatsu, M. Murata, and Y. Murata, “Encapsulation of molecular hydrogen in fullerene C<sub>60</sub> by organic synthesis,” *Science* **307**, 238–240 (2005).
- 2 S. Bloodworth and R. J. Whitby, “Synthesis of endohedral fullerenes by molecular surgery,” *Commun. Chem.* **5**, 121 (2022).

- 3 K. Kurotobi and Y. Murata, “A single molecule of water encapsulated in fullerene C<sub>60</sub>,” *Science* **333**, 613–616 (2011).
- 4 A. Krachmalnicoff, R. Bounds, S. Mamone, S. Alom, M. Concistrè, B. Meier, K. Kouřil, M. E. Light, M. R. Johnson, S. Rols, A. J. Horsewill, A. Shugai, U. Nagel, T. Rõõm, M. Carravetta, M. H. Levitt, and R. J. Whitby, “The dipolar endofullerene HF@C<sub>60</sub>,” *Nat. Chem.* **8**, 953–957 (2016).
- 5 S. Bloodworth, G. Sotinova, S. Alom, S. Vidal, G. R. Bacanu, S. J. Elliott, M. E. Light, J. M. Herniman, G. J. Langley, M. H. Levitt, and R. J. Whitby, “First synthesis and characterization of CH<sub>4</sub>@C<sub>60</sub>,” *Angew. Chem., Int. Ed.* **58**, 5038–5043 (2019).
- 6 S. Bloodworth, G. Hoffman, M. C. Walkey, G. R. Bacanu, J. M. Herniman, M. H. Levitt, and R. J. Whitby, “Synthesis of Ar@C<sub>60</sub> using molecular surgery,” *Chem. Commun.* **56**, 10521–10524 (2020).
- 7 G. Hoffman, M. C. Walkey, J. Gräsvik, G. R. Bacanu, S. Alom, S. Bloodworth, M. E. Light, M. H. Levitt, and R. J. Whitby, “A solid-state intramolecular Wittig reaction enables efficient synthesis of endofullerenes including Ne@C<sub>60</sub>, <sup>3</sup>He@C<sub>60</sub>, and HD@C<sub>60</sub>,” *Angew. Chem., Int. Ed.* **60**, 8960–8966 (2021).
- 8 G. Hoffman, G. R. Bacanu, E. S. Marsden, M. C. Walkey, M. Sabba, S. Bloodworth, G. J. Tizzard, M. H. Levitt, and R. J. Whitby, “Synthesis and <sup>83</sup>Kr NMR spectroscopy of Kr@C<sub>60</sub>,” *Chem. Commun.* **58**, 11284–11287 (2022).
- 9 T. Weiske, T. Wong, W. Krätschmer, J. K. Terlow, and H. Schwarz, “The Neutralization of HeC<sub>60</sub><sup>+</sup> in the gas phase: Compelling evidence for the existence of an endohedral structure for He@C<sub>60</sub>,” *Angew. Chem., Int. Ed.* **31**, 183–185 (1992).
- 10 F. Cimpoesu, S. Ito, H. Shimotani, H. Takagi, and N. Drago, “Vibrational properties of noble gas endohedral fullerenes,” *Phys. Chem. Chem. Phys.* **13**, 9609–9615 (2011).
- 11 G. R. Bacanu, T. Jafari, M. Aouane, J. Rantaharju, M. Walkey, G. Hoffman, A. Shugai, U. Nagel, M. Jiménez-Ruiz, A. J. Horsewill, S. Rols, T. Rõõm, R. J. Whitby, and M. H. Levitt, “Experimental determination of the interaction potential between a helium atom and the interior surface of a C<sub>60</sub> fullerene molecule,” *J. Chem. Phys.* **155**, 144302 (2021).
- 12 A. Takeda, Y. Yokoyama, S. Ito, T. Miyazaki, H. Shimotani, K. Yakigaya, T. Kakiuchi, H. Sawa, H. Takagi, K. Kitazawa, and N. Drago, “Superconductivity of doped Ar@C<sub>60</sub>,” *Chem. Commun.* **2006**, 912–914.
- 13 G. R. Bacanu, J. Rantaharju, G. Hoffman, M. C. Walkey, S. Bloodworth, M. Concistrè, R. J. Whitby, and M. H. Levitt, “An internuclear J-coupling of <sup>3</sup>He induced by molecular confinement,” *J. Am. Chem. Soc.* **142**, 16926–16929 (2020).
- 14 N. Drago, A. M. Flank, P. Lagarde, S. Ito, H. Shimotani, and H. Takagi, “Molecular thermal contraction of the Ar@C<sub>60</sub> endohedral fullerene,” *Phys. Rev. B* **84**, 155448 (2011).
- 15 E. K. Campbell, E. S. Reedy, J. Rademacher, R. J. Whitby, and G. Hoffman, “Electronic spectroscopy of He@C<sub>60</sub><sup>+</sup> for astrochemical consideration,” *Astro-phys. J.* **897**, 88 (2020).
- 16 K. Yamamoto, M. Saunders, A. Khong, R. J. Cross, M. Grayson, M. L. Gross, A. F. Benedetto, and R. B. Weisman, “Isolation and spectral properties of Kr@C<sub>60</sub>, a stable van der Waals molecule,” *J. Am. Chem. Soc.* **121**, 1591–1596 (1999).
- 17 M. S. Syamal, R. J. Cross, and M. Saunders, “<sup>129</sup>Xe NMR spectrum of xenon inside C<sub>60</sub>,” *J. Am. Chem. Soc.* **124**, 6216–6219 (2002).
- 18 M. Frunzi, R. J. Cross, and M. Saunders, “Effect of xenon on fullerene reactions,” *J. Am. Chem. Soc.* **129**, 13343 (2007).
- 19 L. Pang and F. Brisse, “Endohedral energies and translation of fullerene-noble gas clusters G@Cn (G = helium, neon, argon, krypton, and xenon: n = 60 and 70),” *J. Phys. Chem.* **97**, 8562–8563 (1993).
- 20 M. S. Son and Y. K. Sung, “The atom-atom potential. Exohedral and endohedral complexation energies of complexes of X@C<sub>60</sub> between fullerene and rare-gas atoms (X = He, Ne, Ar, Kr, and Xe),” *Chem. Phys. Lett.* **245**, 113–118 (1995).
- 21 H. A. Jiménez-Vázquez and R. J. Cross, “Equilibrium constants for noble-gas fullerene compounds,” *J. Chem. Phys.* **104**, 5589–5593 (1996).
- 22 S. Patchkovskii and W. Thiel, “Equilibrium yield for helium incorporation into buckminsterfullerene: Quantum-chemical evaluation,” *J. Chem. Phys.* **106**, 1796–1799 (1997).
- 23 C. Wang, M. Straka, and P. Pyykkö, “Formulations of the closed-shell interactions in endohedral systems,” *Phys. Chem. Chem. Phys.* **12**, 6187–6203 (2010).
- 24 T. Jafari, G. R. Bacanu, A. Shugai, U. Nagel, M. Walkey, G. Hoffman, M. H. Levitt, R. J. Whitby, and T. Rõõm, “Terahertz spectroscopy of the helium endofullerene He@C<sub>60</sub>,” *Phys. Chem. Chem. Phys.* **24**, 9943–9952 (2022).

- <sup>25</sup>A. L. R. Bug, A. Wilson, and G. A. Voth, "Nonlinear vibrational dynamics of a neon atom in fullerene C<sub>60</sub>," *J. Phys. Chem.* **96**, 7864–7869 (1992).
- <sup>26</sup>S. Flügge, *Practical Quantum Mechanics* (Springer-Verlag, Berlin, 1971), Vol. 1.
- <sup>27</sup>A. Shugai, U. Nagel, Y. Murata, Y. Li, S. Mamone, A. Krachmalnicoff, S. Alom, R. J. Whitby, M. H. Levitt, and T. Rööm, "Infrared spectroscopy of an endohedral water in fullerene," *J. Chem. Phys.* **154**, 124311 (2021).
- <sup>28</sup>F. Leclercq, P. Damay, M. Foukani, P. Chieux, M. C. Bellissent-Funel, A. Rassat, and C. Fabre, "Precise determination of the molecular geometry in fullerene C<sub>60</sub> powder: A study of the structure factor by neutron scattering in a large momentum-transfer range," *Phys. Rev. B* **48**, 2748–2758 (1993).
- <sup>29</sup>J. Meija, T. B. Coplen, M. Berglund, W. A. Brand, P. De Bièvre, M. Gröning, N. E. Holden, J. Irrgeher, R. D. Loss, T. Walczyk, and T. Prohaska, "Isotopic compositions of the elements 2013 (IUPAC Technical Report)," *Pure Appl. Chem.* **88**, 293–306 (2016).
- <sup>30</sup>W. I. F. David, R. M. Ibberson, T. J. S. Dennis, J. P. Hare, and K. Prassides, "Structural phase transitions in the fullerene C<sub>60</sub>," *Europhys. Lett.* **18**, 219–225 (1992).
- <sup>31</sup>P. A. Heiney, "Structure, dynamics and ordering transition of solid C<sub>60</sub>," *J. Phys. Chem. Solids* **53**, 1333–1352 (1992).
- <sup>32</sup>S. Rols, C. Bousige, J. Cambedouzou, P. Launois, J.-L. Sauvajol, H. Schober, V. N. Agafonov, V. A. Davydov, and J. Ollivier, "Unravelling low lying phonons and vibrations of carbon nanostructures: The contribution of inelastic and quasi-elastic neutron scattering," *Eur. Phys. J.: Spec. Top.* **213**, 77–102 (2012).
- <sup>33</sup>P. M. Felker, V. Vlček, I. Hietanen, S. FitzGerald, D. Neuhauser, and Z. Bačić, "Explaining the symmetry breaking observed in the endofullerenes H<sub>2</sub>@C<sub>60</sub>, HF@C<sub>60</sub>, and H<sub>2</sub>O@C<sub>60</sub>," *Phys. Chem. Chem. Phys.* **19**, 31274–31283 (2017).